NANO LETTERS

Letter

pubs.acs.org/NanoLett

Correlating Atomic Structure and Transport in Suspended Graphene Nanoribbons

Zhengqing John Qi,[†,⊥] Julio A. Rodríguez-Manzo,[†,⊥] Andrés R. Botello-Méndez,[‡] Sung Ju Hong,[†,§] Eric A. Stach,[∥] Yung Woo Park,[§] Jean-Christophe Charlier,[‡] Marija Drndić,*[,†] and A. T. Charlie Johnson*[,†]

[†]Department of Physics and Astronomy, University of Pennsylvania, Philadelphia, Pennsylvania 19104, United States

[‡]Institute of Condensed Matter and Nanosciences, Université Catholique de Louvain, Chemin des étoiles 8, 1348 Louvain-la-Neuve, Belgium

[§]Department of Physics and Astronomy, Seoul National University, 1 Gwanak-ro, Gwanak-gu, Seoul, 151-747, Korea

[∥]Center for Functional Nanomaterials, Brookhaven National Laboratory, Upton, New York 11973, United States

S *Supporting Information*

ABSTRACT: Graphene nanoribbons (GNRs) are promising candidates for next generation integrated circuit (IC) components; this fact motivates exploration of the relationship between crystallographic structure and transport of graphene patterned at IC-relevant length scales (<10 nm). We report on the controlled fabrication of pristine, freestanding GNRs with widths as small as 0.7 nm, paired with simultaneous lattice-resolution imaging and electrical transport characterization, all conducted within an aberration-corrected transmission electron microscope. Few-layer GNRs very frequently formed bonded-bilayers and were remarkably robust, sustaining currents in excess of 1.5 μA per carbon bond across a 5 atom-wide ribbon. We found that the intrinsic conductance of a sub-10 nm bonded bilayer GNR scaled with width as $G_{BL}(w) \approx 3/4(e^2/h)w$, where w is the width in nanometers, while a monolayer GNR was roughly five times less conductive. Nanosculpted, crystalline monolayer GNRs exhibited armchair-terminated edges after current annealing, presenting a pathway for the controlled fabrication of semiconducting GNRs with known edge geometry. Finally, we report on simulations of quantum transport in GNRs that are in qualitative agreement with the observations.

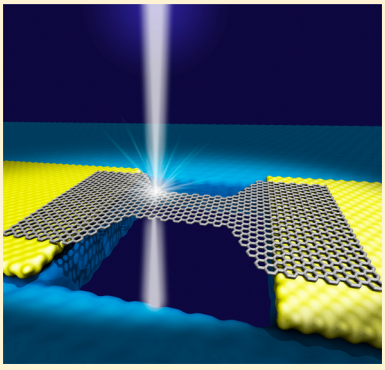

KEYWORDS: *Graphene, electronic transport properties, transmission electron microscopy, graphene nanoribbon, nanofabrication, graphene point contact*

Graphene nanoribbons (GNRs) derived from wafer-scale material are attractive candidates for next-generation integrated circuit (IC) components, for example, on-chip electrical interconnects[1] or transistor channels.[2−4] Despite advances in growth of single-crystal graphene by chemical vapor deposition (CVD),[5,6] the intrinsic properties of patterned GNRs are expected to be degraded by unintentional doping[7−9] and chemical contaminants[10−12] associated with the fabrication process and the substrate. Furthermore, at IC-relevant length scales below 10 nm, edge terminations should play an important role, as they are predicted to determine the band structure[13,14] and electron transport[15] of GNRs. However, experimental verification of these predictions remains a challenge because it requires combining atomic-resolution fabrication and structure determination with transport measurements.

The electron beam of a transmission electron microscope (TEM) can be focused into a spot of a few nanometers in diameter. If its energy is larger than ∼80 keV,[16] it can be used to displace carbon atoms from chosen areas in graphene.[17−20] Nanosculpting of isolated graphene devices was demonstrated within a TEM but the crystallographic orientation and edge structure could not be determined due to resolution limitations.[17] Crack formation induced by electrical biasing within an AC-TEM was used to study the morphology of narrow graphene constrictions[21,22] but this approach does not provide a pathway for deterministic patterning. To date, controlled patterning in an aberration-corrected TEM has not been utilized to define device structures that could then be biased in situ. A clear correlation between the subnanometer structure and electrical properties of systematically patterned GNRs could provide greater insight into graphene's relevance for future nanoelectronics.

Here we report the fabrication, lattice-resolution imaging, and electrical characterization of pristine mono- and few-layer GNRs with widths below 10 nm, performed in situ within an AC-TEM. Bonded bilayer GNRs were controllably fabricated with widths as low as 0.7 nm, and they supported current densities in excess of 4×10^9 A/cm^2, 3 orders of magnitude

Received: February 25, 2014

   dx.doi.org/10.1021/nl501872x | *Nano Lett.* XXXX, XXX, XXX−XXX

greater than state-of-the-art interconnects. Monolayer GNRs formed by nanosculpting followed by current annealing were consistently observed to have armchair-terminated edges, presenting a pathway for fabricating edge-specific GNRs. We found that the GNR conductance scaled approximately as $G_{BL}(w) \approx 3/4\ (e^2/h)w$ for a bonded-bilayer GNR and $G_{ML}(w) \approx {}^3/_{20}\ (e^2/h)w$ for a monolayer GNR, where w is the width in nanometers. The high conductance of the bonded-bilayer GNR is attributed to sp^2-bonded edges that stabilize the structure[23−25] and distribute current into additional conduction channels. Quantum transport simulations of the conductance were in qualitative agreement with the measurements. The work represents a systematic approach to study the interplay between atomic structure and electronic properties of GNRs and provides a pathway for future studies in novel two-dimensional materials such as dichalcogenides and nitrides.

Details of the fabrication process can be found in the Supporting Information. Figure 1a shows an optical micrograph

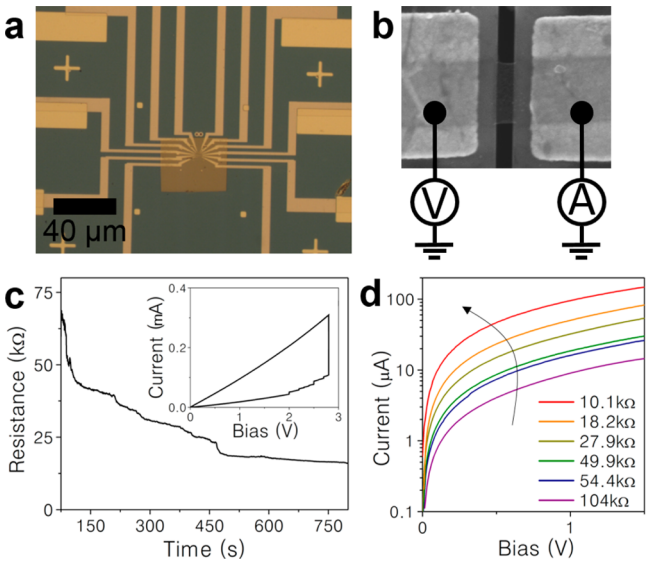

Figure 1. Device layout and current annealing procedure. (a) Optical micrograph of TEM-compatible chip with multiple electrodes converging onto a silicon nitride membrane. (b) SEM micrograph of suspended 500 nm wide graphene ribbon. (c) Time evolution of device resistance during current annealing. Inset: Corresponding current versus bias voltage measurement for the same device. (d) Current-bias voltage sweeps for a single device after multiple annealing steps, which cause the resistance to decrease from 104 to 10 kΩ.

of a TEM-compatible chip with multiple source-drain electrodes that contact an array of two-terminal devices on a 100 nm-thick SiN_x membrane (Figure 1a). Each device consisted of a 500 nm wide strip of graphene bridging an electrode pair with a graphene region suspended over a 150 nm slit (Figures 1b and 2a). Devices were based on both few- and monolayer graphene grown by atmospheric pressure CVD.[26] Samples were mounted on a TEM holder with electrical feedthroughs (Protochips Inc.) to allow for in situ electrical transport measurements. TEM experiments were performed in either a FEI-Titan with corrected spherical aberrations, operating with a beam accelerating voltage of 80 or 300 keV, or in a JEOL 2010F operating at 200 kV (in this case experiments relied on a homemade TEM holder with electrical feedthroughs[17]).

Once the devices were in the TEM, a slow voltage ramp (typically 0−2.8 V at 5 mV/s) was used to induce Joule heating that removed contaminants associated with lithographic processing. The electrical resistance decreased from ∼100 kΩ for as-fabricated devices to ∼10 kΩ after the cleaning step (Figure 1c,d), which was attributed to removal of resist residue and improved contact resistance due to heating. After this step, the sample surface was very clean, and electron diffraction data were consistent with single crystal graphene grains with dimensions of at least 100 nm in diameter (Figure 2a−c) for both mono- and few-layer samples (see Figure S1 in the Supporting Information).

Cleaned devices were further patterned by nanosculpting using the TEM electron beam. The electron beam (with beam energy of 200 or 300 keV, well above 80 keV, the threshold for knock-on damage in graphitic materials[16,27,28]) was focused to a spot (diameter <5 nm) and then moved to progressively sculpt the suspended graphene to widths less than 10 nm by ejecting carbon atoms from the lattice (inset of Figure 2d). During nanosculpting, the voltage bias was held at 1−3 V to induce Joule heating that prevented electron-beam induced hydrocarbon contamination[29] and damage accumulation[30] and allowed for healing of atomic defects,[31] so that the few-layer (Figure 3a−d) and monolayer (Figure 4a−d) GNRs remained highly crystalline.[17,32,33] This procedure was used to successively narrow the width of the GNRs from 500 nm to ca. 10 nm. An example of in situ electrical measurement during the nanosculpting procedure is shown in Figure 2d. The sample resistance increased as the GNR width was reduced during nanosculpting (Figure 2e). Plateaus in the resistance indicate a pause in sculpting when the GNR was imaged. With this patterning technique, we measured the resistance as a function of width for few-layer and monolayer GNRs over the range 10−500 nm (Figure 2f). For each sample, the data were well fit by the form appropriate for an Ohmic conductor in series with a contact resistance: $R_{TOT} = R_C + \rho/w$, where R_C is the contact resistance, w is the width of the GNR, and ρ is a fit parameter with units of resistance multiplied by length. The contact resistance is assumed to reflect the resistance of the wiring, the metal−graphene interface, and wider graphene regions away from the GNR. The contact resistances inferred from the fits were 9.7 ± 0.2 and 11.4 ± 0.3 kΩ for few-layer GNRs and 18.9 ± 0.5 and 24.4 ± 0.5 kΩ for monolayer GNRs, consistent with the expectation that few-layer graphene structures should be less resistive, all other aspects being similar. The structural and electrical analysis of mono- and few-layer GNR devices with widths less than 10 nm are discussed in the following paragraphs.

Nanosculpting was not utilized for narrowing GNRs to widths below 10 nm, because it was desirable to have uninterrupted imaging as the sample width was reduced. To enable this, sub-10 nm dimensions were achieved by application of electrical stress to GNRs, which led to a reduction of width due to changes in the atomic lattice.[34] Sputtering of atoms can also occur at the beam energies used, however the current density of the beam alone cannot account for the structural changes observed during the experiment (see Supporting Information for calculation of sputtering rate). In these experiments, few-layer GNRs were observed to consist of stacks of bonded graphene bilayers, which exhibit a dark edge contrast (Figures 3a−d and S2 in the Supporting Information) consistent with previous observations on heated graphene sheets.[23,34] Figure 3e presents supporting evidence that the dark edges seen in few-layer GNRs represent a bonded edge. Corresponding two-dimensional fast Fourier transform (2D

dx.doi.org/10.1021/nl501872x | Nano Lett. XXXX, XXX, XXX−XXX

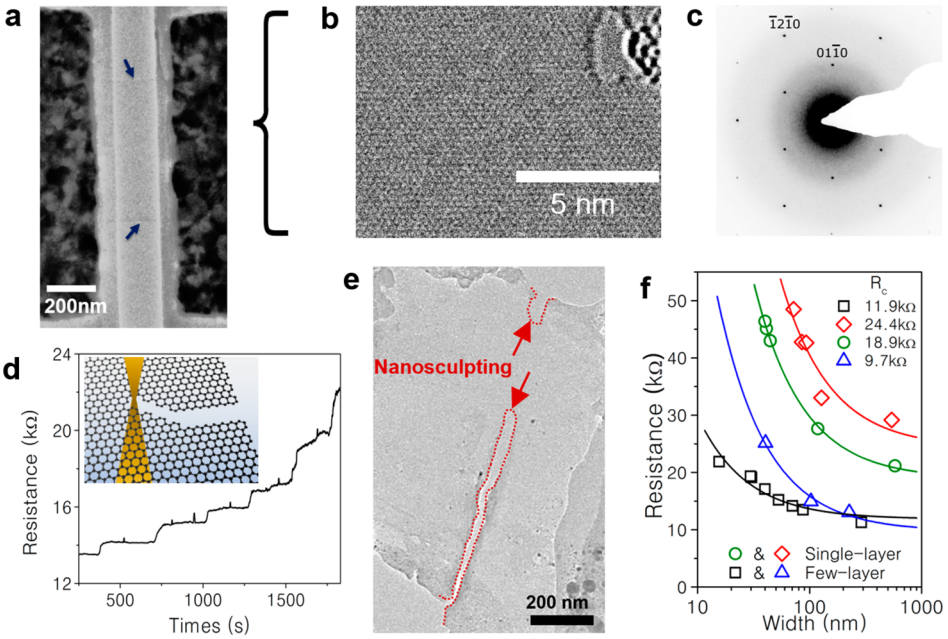

Figure 2. Nanosculpting of suspended graphene using a focused TEM beam. (a) TEM image of initial free-standing 500 nm wide GNR contacted by Au electrodes. Arrows indicate the edges of the ribbon. (b) Corresponding high-resolution TEM micrograph of a monolayer GNR after cleaning, showing a nearly pristine surface. (c) Electron diffraction pattern taken from a 100 nm-diameter area of a clean GNR. (d) Time evolution of GNR resistance during sculpting. Steplike increases in resistance represent periods of sculpting (narrowing of the GNR) while plateaus represent pauses in sculpting when the beam is blanked. Inset: Schematic of sculpting technique.[17] (e) TEM micrograph of graphene after nanosculpting with the sculpted region highlighted in red and indicated by arrows. (f) Two-terminal GNR resistance as a function of width (w) for w > 10 nm with solid curves showing fits of the form $R_{TOT} = R_C + R_M/w$ with w measured in nanometers.

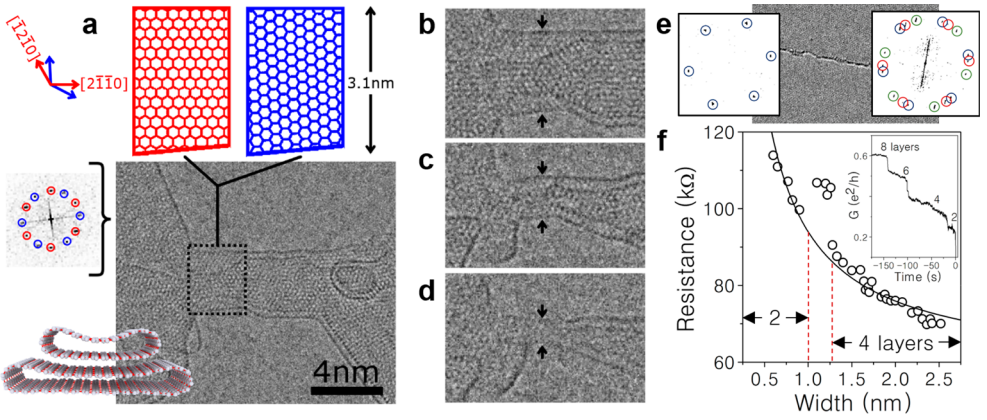

Figure 3. Layer-by-layer electrical stress-induced fracturing of a GNR consisting of two stacked, bonded graphene bilayers and correlated transport properties. (a) High-resolution micrograph of the GNR with bonded bilayers of width w = 3.2 and 1.2 nm. (b) Narrowing of the GNR. (c) Image of the GNR immediately after breaking of the top-bonded bilayer. (d) Final structure, showing a single bonded-bilayer GNR with a width of 0.7 nm, immediately before the GNR ruptured. Images (b−d) are 1.5× larger than (a). (e) TEM micrograph of a trilayer graphene sheet (top) and a single-layer graphene sheet (bottom) separated by a single sp^2-bonded edge. Number of layers is extracted from the 2D FFT of each region of the image. (f) Few-layer GNR resistance as a function of width and the best fit to the data (black line) $R_{TOT} = R_C + \rho/w$ with w the width in nanometers. Here R_C = 58 kΩ and ρ = 36 kΩ-nm. Inset: Time evolution of GNR conductance with step-like drops indicating the breaking of bonded bilayers until eventual failure (at t = 0 s).

FFT), showing the spatial frequencies present in the image and their orientations, were taken for the regions above (Figure 3e right inset) and below (Figure 3e left inset) the dark line in Figure 3e. The lower region in the image is a monolayer sheet (signified by a set of 6-fold peaks representing 1/0.213 nm^{-1} spatial frequencies and therefore {1−100} planes) while the top contains three layers (indicated by three rotated sets of 6-fold peaks in the FFT). The single dark interface represents a bonded edge, delineating the mono- and trilayer regions (for higher resolution, see Figure S3 in the Supporting Information). In contrast, free edges of graphene monolayers showed low contrast in high-resolution TEM images (Figure 4a−d), enabling the two cases to be distinguished.

The 2D FFT of TEM images were also used to determine the crystallographic orientation of individual graphene layers and layer edges. Consider, for example, the GNR of Figure 3a, which consisted of a stack of two bonded bilayers with minimum widths of 3.2 and 1.2 nm. After the narrower bilayer ruptured (Figure 3c), the structure of the wider bilayer was determined; the measured width of the bilayer and the rotation

dx.doi.org/10.1021/nl501872x | Nano Lett. XXXX, XXX, XXX−XXX

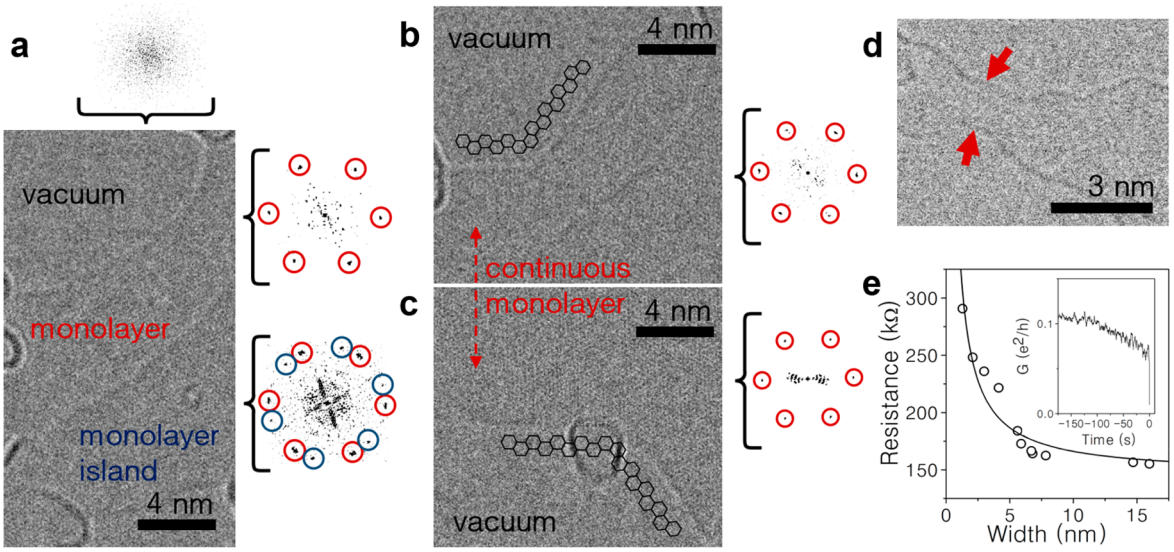

Figure 4. Edge morphology and transport of single-layer GNRs. (a) TEM micrograph of a single-layer GNR edge immediately after nanosculpting, showing a curved edge. An isolated monolayer graphene island is observed on an underlying monolayer. The 2D FFTs for vacuum (top), underlying monolayer, and the island region are provided. (b) Evolution of (a) after current annealing showing the formation of armchair edges along the top edge of the GNR. Corresponding 2D FFT is to the right. (c) The lower edge of the GNR with corresponding 2D FFT to the right, indicative of an armchair edge geometry. (d) TEM image of an isolated single-layer GNR (w = 1.3 nm). (e) Resistance as a function of width for monolayer GNR. Solid black curve is a fit to the form $R_{TOT} = R_C + \rho/w$ with R_C = 145 kΩ and ρ = 207 kΩ-nm. Inset: Time evolution of monolayer GNR conductance until device breakdown at t = 0 s.

between the layers of 27° inferred from the 2D FFT were used to create an atomistic model (top part of Figure 3a), which was then used for simulations discussed below. On the basis of the geometry, transport occurred parallel to the $[2\bar{1}\bar{1}0]$ direction for one layer and close to the $[10\bar{1}0]$ direction for the second. Immediately before the bilayer GNR ruptured, its width was 0.7 nm (Figure 3d), corresponding to roughly the distance of three $(01\bar{1}0)$ lattice planes, and it supported a current density of 4×10^9 A/cm^2, or 1.5 μA per carbon bond. Video 1 in the Supporting Information provides the entire TEM series.

Monolayer GNRs presented a curved edge immediately after nanosculpting (Figure 4a) that recrystallized into a faceted edge after current annealing (Figure 4b). In this case, the 2D FFT was used to determine the GNR structure as well as the edge orientation before (Figure 4a) and after current annealing (Figure 4b,c). From this analysis, we conclude that the lattice orientation is unchanged by current annealing, and that the straight edges present after current annealing are oriented along the armchair lattice direction for both the top (Figure 4b) and bottom edge (Figure 4c). This finding is consistent with theoretical predictions[29,33,35] that the armchair edge configuration has the lowest energy per atom. The approach of nanosculpting followed by current annealing thus provides a pathway to fabrication of semiconducting monolayer GNRs with well-defined (armchair) edge geometry. Along with the structural analysis provided above, the focus of the current work is the width dependence of the GNR conductance as well as the maximum sustained current density.

Electrical stress was used to narrow monolayer GNRs to widths below 10 nm, similar to the narrowing of few-layer GNR discussed above. A monolayer GNR of w = 1.3 nm is shown in Figure 4d; this image was taken at low beam current densities to reduce knock-on damage. For this very narrow monolayer GNR, lattice resolution was not achieved due to mechanical instability of the sample, however we expect that armchair edges dominate, as found for wider monolayer GNRs (Figure 4b).

The four-layer GNR shown in Figure 3a–e was put under electrical stress until failure, as described above. The electrical conductance and width of the GNR were monitored through the process (see Figure 3f). A jump in resistance is observed at a width of 1.2 nm, corresponding to the breaking of the first bonded bilayer (seen in Figure 3c). We fit the resistance to the form $R_{TOT} = R_C + \rho/w$, excluding the resistance spike region (black curve in Figure 3f) and found best fit values R_C = 58 ± 1 kΩ and ρ = 36 ± 1 kΩ-nm. The same fit was found to apply in both the four-layer and bilayer region, suggesting that conduction was predominantly via the wider bilayer (for that reason, we refer to the sample as a bonded-bilayer from this point forward). For the monolayer case, a similar fitting procedure was used to analyze the data (black curve in Figure 4e), and the best fit parameters were R_C = 145 ± 6 kΩ and ρ = 207 ± 20 kΩ-nm. For both samples, the inferred contact resistance in the sub-10 nm regime was significantly larger than that found for the measurements summarized in Figure 2f. In each case, the intrinsic conductance of the GNR as a function of width was calculated (i.e., ignoring the contact resistance) and found to scale linearly with width (measured in nanometers); for the bonded-bilayer GNR, $G_{BL}(w) \approx 0.75\ (e^2/h)w$[nm], while the intrinsic conductance of the monolayer GNR was approximately five times lower, $G_{ML}(w) \approx 0.15\ (e^2/h)w$[nm] (see Figure 5a). The lower inferred value of R_C in the bonded-bilayer GNR is ascribed to increased conduction paths in the multilayer graphene leads and reduced scattering associated with sp^2 edge bonding compared to free edges of the monolayer. The enhanced conductance of the bonded-bilayer sample suggests that similar devices would be more suitable for use as on-chip interconnects. The bonded-bilayer GNR also sustained a very large maximum current density of 4.2×10^9 A/cm^2, 3 orders of magnitude than that of state-of-the-art interconnects, even when its width was just 0.7 nm.

dx.doi.org/10.1021/nl501872x | Nano Lett. XXXX, XXX, XXX−XXX

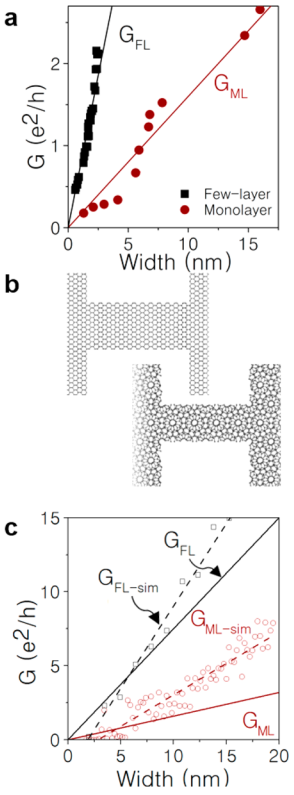

Figure 5. Conductance scaling of GNRs. (a) Measured conductance as a function of width for few-layer (black squares) and monolayer (red circles) GNRs, after subtraction of the best fit contact resistance. The black line is a fit of the form $G_{FL}(w) \approx 0.75\ (e^2/h)w$[nm], and the red line is a fit of the form $G_{ML}(w) = 0.15\ (e^2/h)w$[nm]. (b) Ball and stick models of armchair-edge monolayer (top) and bonded bilayer (bottom) GNR devices used for quantum transport calculations. (c) Conductance as a function of width for simulated and measured GNRs. Black (red) data points are from simulations of the conductance of bonded bilayer (armchair-edge monolayer) GNR with dashed lines as corresponding linear fits. Solid lines represent linear fits to the experimental data, as reproduced from panel (a).

Quantum conductance calculations were conducted and compared to the measurements in order to develop a quantitative understanding of the intrinsic properties of bonded-bilayer and monolayer GNRs. The simulations were performed on systems with geometries inferred from experimental TEM images. The simulation included a channel region ca. 5 nm in length, placed between wide (ca. 30 nm) nanoribbons serving as leads (see Supporting Information for simulation methodology). On the basis of experimentally obtained structural information (Figures 3a and 4a,b), the channel constriction region consisted of either a bonded bilayer with a layer twist of 26.4° or monolayer with an armchair edge (Figure 5b). Any difference between the twist angle in the simulation and that determined from TEM data (27°) is not expected to lead to a significant effect since the variation of conductance with twist is weak when close to either AA or AB stacking (i.e., $\theta \sim 0$ or $\theta \sim 30°$).[36]

For the case of a semi-infinite monolayer GNR, the conductance as a function of carrier energy, $G(E)$, increases in a stepwise manner as additional conduction channels are accessed (Figure S4 of the Supporting Information). In contrast, for a monolayer GNR contacted by wider leads as in the experiment, $G(E)$ exhibits oscillations at low carrier energies due to interference and scattering at the constriction.[37] For the bonded bilayer case, the number of channels is effectively doubled, and the average conductance increases. Conductance oscillations again occur at low energies due to interference effects. Above a carrier energy threshold, oscillations are suppressed due to increased conduction via interband tunneling.

The width-dependent conductance at constant carrier energy $G(E = E_0, w)$ for an ideal, semi-infinite GNR exhibits a series of quantized conductance steps as the width narrows, consistent with limiting the number of accessible channels (Figure S5 in the Supporting Information). To compare with experiment, the carrier energy was taken to be 0.6 eV corresponding to the bias voltage used in the experiments. For the case of a GNR constriction between wider leads, the steps are washed out by contact effects (i.e., reflection and scattering), and $G(w)$ exhibits a near-linear behavior, consistent with the experiment. In this case, $G_{BL\text{-}sim}(w) \sim 1.1\ (e^2/h)w$ for bonded bilayer GNRs and $G_{ML\text{-}sim}(w) \sim 0.4\ (e^2/h)w$ for monolayer GNRs (Figure 5c). In the simulation, the conductance drops to zero for $w < 2$ nm due to a quantum-confinement energy gap that exceeds the carrier energy.

The agreement between experiment and simulation is very good. In both experiment and simulation, bonded-bilayer GNRs exhibit higher conductance than monolayer GNRs due to the presence of additional conduction channels and reduced carrier scattering in the bilayer. The measured enhancement for bilayer GNRs is a factor of 5, while the enhancement in simulation is a factor of 3. Surprisingly, the experiments did not show conductance suppression or other evidence of an energy gap in samples with $w < 2$ nm as predicted theoretically. This can be attributed to several factors. First, the chemical potential could lie outside the energy gap due to unintentional carrier doping, allowing for conduction even at narrow widths. Alternatively, the explanation may lie in transport processes not included in the simulation, for example, inelastic phonon scattering effects or tunneling through the narrowest part of the constriction where the energy gap is present. It has been predicted that different contact angles and junctions can modulate the ribbon to have near perfect transmissions or zero conductance,[36,38,39] which could account for the discrepancy from theory because a 90° contact angle is assumed. Finally, mechanical stress in the system could lead to the tuning of the energy gap,[40] which was not accounted for in the simulation. Future work implementing a third terminal to modulate the chemical potential will provide greater insight on the electronic structure of these GNRs and enable enhanced comparison with computational work.

In summary, we have demonstrated the controlled fabrication of mono- and few-layer GNRs with correlated lattice resolution imaging and electrical biasing, down to widths of 0.7 nm. We measured the electrical properties of GNRs for widths less than 15 nm and found that conductance scaled approximately as $G_{FL}(w) \approx 0.75\ (e^2/h)w$[nm] for a bilayer GNR and $G_{ML}(w) \approx 0.15\ (e^2/h)w$[nm] for a monolayer GNR. The high conductance in few-layer GNRs is enabled by their bonded edges, which provided structural stability and additional conduction channels, allowing for sustained currents in excess of 1.5 μA per carbon bond. Monolayer GNRs formed armchair-terminated edges after current annealing, presenting a pathway for fabricating edge-specific GNRs. The methodology presented here should enable future experiments to correlate sample conductance with atomic geometry in emerging two-

dx.doi.org/10.1021/nl501872x | Nano Lett. XXXX, XXX, XXX–XXX

dimensional materials such as layered transition metal dichalcogenides and nitrides.

■ ASSOCIATED CONTENT

Supporting Information

Details of the device fabrication, method used for quantum transport calculations, and calculations for the sputtering rate of C atoms from the electron beam are provided. In addition, supporting TEM data on edge bonding and calculated quantum conductance of different GNR devices are available. This material is available free of charge via the Internet at http://pubs.acs.org.

■ AUTHOR INFORMATION

Corresponding Authors

*E-mail: (M.D.) drndic@physics.upenn.edu.
*E-mail: (A.T.C.J.) cjohnson@physics.upenn.edu.

Author Contributions

⊥Z.J.Q. and J.A.R.-M. contributed equally to this work.

Notes

The authors declare no competing financial interest.

■ ACKNOWLEDGMENTS

This work was supported by SRC contract no. 2011-IN-2229, which is associated with the NSF AIR Program ENG-1312202. M.D. and J.A.R.-M. acknowledge funding from the NIH Grant R21HG006313 and the Nano/Bio Interface Center through the National Science Foundation NSEC DMR08-32802. Research was carried out in part at the Center for Functional Nanomaterials, Brookhaven National Laboratory, which is supported by the U.S. Department of Energy, Office of Basic Energy Sciences, under Contract No. DE-AC02-98CH10886. We acknowledge support for access of the FEI-Titan ACTEM through proposal 31972 at Brookhaven National Laboratory's Center for Functional Nanomaterials. Y.W.P. and S.J.H. acknowledge support from the Leading Foreign Research Institute Recruitment Program (0409-20100156) of NRF and the FPRD of BK21 through the MEST, Korea. A.R.B-M. and J-C.C. acknowledge financial support from the F.R.S.-FNRS of Belgium, from the Communauté Française de Belgique and the European ICT FET Flagship entitled "Graphene-based revolutions in ICT and beyond" through the ARC on "Graphene Nanoelectromechanics" (no. 11/16-037). Computational resources were provided by the CISM of the Université catholique de Louvain.

■ REFERENCES

(1) Behnam, A.; Lyons, A. S.; Bae, M. H.; Chow, E. K.; Islam, S.; Neumann, C. M.; Pop, E. Transport in Nanoribbon Interconnects Obtained from Graphene Grown by Chemical Vapor Deposition. *Nano Lett.* **2012**, *12*, 4424−4430.

(2) Han, M. Y.; Ozyilmaz, B.; Zhang, Y.; Kim, P. Energy Band Gap Engineering of Graphene Nanoribbons. *Phys. Rev. Lett.* **2007**, *98*, 206805.

(3) Hwang, W. S.; Tahy, K.; Li, X.; Xing, H.; A.C, S.; Sung, C. Y.; Jena, D. Transport Properties of Graphene Nanoribbon Transistors on Chemical-Vapor-Deposition Grown Wafer-Scale Graphene. *Appl. Phys. Lett.* **2012**, *100*, 203107.

(4) Chen, Z.; Lin, Y.-M.; Rooks, M. J.; Avouris, P. Graphene Nano-Ribbon Electronics. *Phys. E* **2007**, *40*, 228−232.

(5) Zhou, H. L.; Yu, W. J.; Liu, L. X.; Cheng, R.; Chen, Y.; Huang, X. Q.; Liu, Y.; Wang, Y.; Huang, Y.; Duan, X. F., Chemical Vapour Deposition Growth of Large Single Crystals of Monolayer and Bilayer Graphene. *Nat. Commun.* **2013**, *4*.

(6) Hao, Y. F.; Bharathi, M. S.; Wang, L.; Liu, Y. Y.; Chen, H.; Nie, S.; Wang, X. H.; Chou, H.; Tan, C.; Fallahazad, B.; et al. The Role of Surface Oxygen in the Growth of Large Single-Crystal Graphene on Copper. *Science* **2013**, *342*, 720−723.

(7) Ni, Z. H.; Yu, T.; Luo, Z. Q.; Wang, Y. Y.; Liu, L.; Wong, C. P.; Miao, J. M.; Huang, W.; Shen, Z. X. Probing Charged Impurities in Suspended Graphene Using Raman Spectroscopy. *ACS Nano* **2009**, *3*, 569−574.

(8) Wehling, T. O.; Novoselov, K. S.; Morozov, S. V.; Vdovin, E. E.; Katsnelson, M. I.; Geim, A. K.; Lichtenstein, A. I. Molecular Doping of Graphene. *Nano Lett.* **2008**, *8*, 173−177.

(9) Caridad, J. M.; Rossella, F.; Bellani, V.; Maicas, M.; Patrini, M.; Diez, E., Effects of Particle Contamination and Substrate Interaction on the Raman Response of Unintentionally Doped Graphene. *J. Appl. Phys.* **2010**, *108*.

(10) Ishigami, M.; Chen, J. H.; Cullen, W. G.; Fuhrer, M. S.; Williams, E. D. Atomic Structure of Graphene on SiO_2. *Nano Lett.* **2007**, *7*, 1643−1648.

(11) Dan, Y.; Lu, Y.; Kybert, N. J.; Luo, Z.; Johnson, A. T. C. Intrinsic Response of Graphene Vapor Sensors. *Nano Lett.* **2009**, *9*, 1472−1475.

(12) Lin, Y. C.; Lu, C. C.; Yeh, C. H.; Jin, C. H.; Suenaga, K.; Chiu, P. W. Graphene Annealing: How Clean Can It Be? *Nano Lett.* **2012**, *12*, 414−419.

(13) Nakada, K.; Fujita, M.; Dresselhaus, G.; Dresselhaus, M. S. Edge State in Graphene Ribbons: Nanometer Size Effect and Edge Shape Dependence. *Phys. Rev. B* **1996**, *54*, 17954−17961.

(14) Ritter, K. A.; Lyding, J. W. The Influence of Edge Structure on the Electronic Properties of Graphene Quantum Dots and Nanoribbons. *Nat. Mater.* **2009**, *8*, 235−242.

(15) Fujita, M.; Wakabayashi, K.; Nakada, K.; Kusakabe, K. Peculiar Localized State at Zigzag Graphite Edge. *J. Phys. Soc. Jpn.* **1996**, *65*, 1920−1923.

(16) Meyer, J. C.; Eder, F.; Kurasch, S.; Skakalova, V.; Kotakoski, J.; Park, H. J.; Roth, S.; Chuvilin, A.; Eyhusen, S.; Benner, G., et al., Accurate Measurement of Electron Beam Induced Displacement Cross Sections for Single-Layer Graphene. *Phys. Rev. Lett.* **2012**, *108*.

(17) Lu, Y.; Merchant, C. A.; Drndic, M.; Johnson, A. T. C. In Situ Electronic Characterization of Graphene Nanoconstrictions Fabricated in a Transmission Electron Microscope. *Nano Lett.* **2011**, *11*, 5184−5188.

(18) Fischbein, M. D.; Drndic, M., Electron Beam Nanosculpting of Suspended Graphene Sheets. *Appl. Phys. Lett.* **2008**, *93*.

(19) Borrnert, F.; Fu, L.; Gorantla, S.; Knupfer, M.; Buchner, B.; Rummeli, M. H. Programmable Sub-Nanometer Sculpting of Graphene with Electron Beams. *ACS Nano* **2012**, *6*, 10327−10334.

(20) Xu, Q.; Wu, M. Y.; Schneider, G. F.; Houben, L.; Malladi, S. K.; Dekker, C.; Yucelen, E.; Dunin-Borkowski, R. E.; Zandbergen, H. W. Controllable Atomic Scale Patterning of Freestanding Monolayer Graphene at Elevated Temperature. *ACS Nano* **2013**, *7*, 1566−1572.

(21) Barreiro, A.; Borrnert, F.; Rummeli, M. H.; Buchner, B.; Vandersypen, L. M. K. Graphene at High Bias: Cracking, Layer by Layer Sublimation, and Fusing. *Nano Lett.* **2012**, *12*, 1873−1878.

(22) Borrnert, F.; Barreiro, A.; Wolf, D.; Katsnelson, M. I.; Buchner, B.; Vandersypen, L. M. K.; Rummeli, M. H. Lattice Expansion in Seamless Bilayer Graphene Constrictions at High Bias. *Nano Lett.* **2012**, *12*, 4455−4459.

(23) Liu, Z.; Suenaga, K.; Harris, P. J. F.; Iijima, S. Open and Closed Edges of Graphene Layers. *Phys. Rev. Lett.* **2009**, 102.

(24) Zheng, Y. P.; Wei, N.; Fan, Z. Y.; Xu, L. Q.; Huang, Z. G. Mechanical Properties of Grafold: A Demonstration of Strengthened Graphene. *Nanotechnology* **2011**, *22*, 405701.

(25) Cruz-Silva, E.; Botello-Mendez, A. R.; Barnett, Z. M.; Jia, X.; Dresselhaus, M. S.; Terrones, H.; Terrones, M.; Sumpter, B. G.; Meunier, V. Controlling Edge Morphology in Graphene Layers Using Electron Irradiation: From Sharp Atomic Edges to Coalesced Layers Forming Loops. *Phys. Rev. Lett.* **2010**, *105*, 045501.

(26) Luo, Z.; Lu, Y.; Singer, D. W.; Berck, M. E.; Somers, L. A.; Goldsmith, B. R.; Johnson, A. T. C. Effect of Substrate Roughness and

Feedstock Concentration on Growth of Wafer-Scale Graphene at Atmospheric Pressure. *Chem. Mater.* **2011**, *23*, 1441−1447.
(27) Smith, B. W.; Luzzi, D. E. Electron Irradiation Effects in Single Wall Carbon Nanotubes. *J. Appl. Phys.* **2001**, *90*, 3509−3515.
(28) Warner, J. H.; Rummeli, M. H.; Ge, L.; Gemming, T.; Montanari, B.; Harrison, N. M.; Buchner, B.; Briggs, G. A. D. Structural Transformations in Graphene Studied with High Spatial and Temporal Resolution. *Nat. Nanotechnol.* **2009**, *4*, 500−504.
(29) Song, B.; Schneider, G. F.; Xu, Q.; Pandraud, G.; Dekker, C.; Zandbergen, H. Atomic-Scale Electron-Beam Sculpting of near-Defect-Free Graphene Nanostructures. *Nano Lett.* **2011**, *11*, 2247−2250.
(30) Krasheninnikov, A. V.; Banhart, F. Engineering of Nanostructured Carbon Materials with Electron or Ion Beams. *Nat. Mater.* **2007**, *6*, 723−733.
(31) Gao, T.; Gao, Y. B.; Chang, C. Z.; Chen, Y. B.; Liu, M. X.; Xie, S. B.; He, K.; Ma, X. C.; Zhang, Y. F.; Liu, Z. F. Atomic-Scale Morphology and Electronic Structure of Manganese Atomic Layers Underneath Epitaxial Graphene on SiC(0001). *ACS Nano* **2012**, *6*, 6562−6568.
(32) Jia, X. T.; Hofmann, M.; Meunier, V.; Sumpter, B. G.; Campos-Delgado, J.; Romo-Herrera, J. M.; Son, H. B.; Hsieh, Y. P.; Reina, A.; Kong, J.; et al. Controlled Formation of Sharp Zigzag and Armchair Edges in Graphitic Nanoribbons. *Science* **2009**, *323*, 1701−1705.
(33) Westenfelder, B.; Meyer, J. C.; Biskupek, J.; Kurasch, S.; Scholz, F.; Krill, C. E.; Kaiser, U. Transformations of Carbon Adsorbates on Graphene Substrates under Extreme Heat. *Nano Lett.* **2011**, *11*, 5123−5127.
(34) Huang, J. Y.; Ding, F.; Yakobson, B. I.; Lu, P.; Qi, L.; Li, J. In Situ Observation of Graphene Sublimation and Multi-Layer Edge Reconstructions. *Proc. Natl. Acad. Sci. U.S.A.* **2009**, *106*, 10103−10108.
(35) Koskinen, P.; Malola, S.; Hakkinen, H., Self-Passivating Edge Reconstructions of Graphene. *Phys. Rev. Lett.* **2008**, *101*.
(36) Botello-Mendez, A. R.; Cruz-Silva, E.; Romo-Herrera, J. M.; Lopez-Urias, F.; Terrones, M.; Sumpter, B. G.; Terrones, H.; Charlier, J. C.; Meunier, V. Quantum Transport in Graphene Nanonetworks. *Nano Lett.* **2011**, *11*, 3058−3064.
(37) Darancet, P.; Olevano, V.; Mayou, D., Coherent Electronic Transport through Graphene Constrictions: Subwavelength Regime and Optical Analogy. *Phys. Rev. Lett.* **2009**, *102*.
(38) Areshkin, D. A.; White, C. T. Building Blocks for Integrated Graphene Circuits. *Nano Lett.* **2007**, *7*, 3253−3259.
(39) Yamamoto, M.; Wakabayashi, K., Control of Electric Current by Graphene Edge Structure Engineering. *Appl. Phys. Lett.* **2009**, *95*.
(40) Sun, L.; Li, Q. X.; Ren, H.; Su, H. B.; Shi, Q. W.; Yang, J. L. Strain Effect on Electronic Structures of Graphene Nanoribbons: A First-Principles Study. *J. Chem. Phys.* **2008**, *129*, 074704.